3-3-2015

Impact of Homogeneous Strain On Uranium Vacancy Diffusion In Uranium Dioxide

Anuj Goyal
University of Florida

Simon R. Phillpot
University of Florida

Gopinath Subramanian
University of Southern Mississippi

David A. Andersson
Los Alamos National Laboratory Materials Science and Technology Division

Chris R. Stanek
Los Alamos National Laboratory Materials Science and Technology Division

See next page for additional authors

Impact of homogeneous strain on uranium vacancy diffusion in uranium dioxide

Anuj Goyal* and Simon R. Phillpot
Department of Materials Science and Engineering, University of Florida, Gainesville, FL 32611, USA

Gopinath Subramanian
School of Polymers and High Performance Materials, University of Southern Mississippi, Hattiesburg, MS 39402

David A. Andersson, Chris R. Stanek, and Blas P. Uberuaga†
Materials Science and Technology Division, Los Alamos National Laboratory, Los Alamos, NM 87545 USA

(Dated: February 13, 2015)

We present a detailed mechanism of, and the effect of homogeneous strains on, the migration of uranium vacancies in UO_2. Vacancy migration pathways and barriers are identified using density functional theory (DFT) and the effect of uniform strain fields are accounted for using the dipole tensor approach. We report complex migration pathways and non-cubic symmetry associated with the uranium vacancy in UO_2 and show that these complexities need to be carefully accounted for to predict the correct diffusion behavior of uranium vacancies. We show that under homogeneous strain fields, only the dipole tensor of the saddle with respect to the minimum is required to correctly predict the change in the energy barrier between the strained and the unstrained case. Diffusivities are computed using kinetic Monte Carlo (KMC) simulations for both neutral and fully charged state of uranium single and di-vacancies. We calculate the effect of strain on migration barriers in the temperature range 800 –1800 K for both vacancy types. Homogeneous strains as small as 2% have a considerable effect on diffusivity of both single and di-vacancies of uranium, with the effect of strain being more pronounced for single vacancies than di-vacancies. In contrast, the response of a given defect to strain is less sensitive to changes in the charge state of the defect. Further, strain leads to anisotropies in the mobility of the vacancy and the degree of anisotropy is very sensitive to the nature of the applied strain field for strain of equal magnitude. Our results suggest that the influence of strain on vacancy diffusivity will be significantly greater when single vacancies dominate the defect structure, such as sintering, while the effects will be much less substantial under irradiation conditions where di-vacancies dominate.

I. INTRODUCTION

Uranium dioxide (UO_2) is the ubiquitous nuclear fuel, whose properties play a key role in the reliability and safety of nuclear reactors.[1–3] As a ceramic insulator/wide-band semiconductor (having a bandgap of 2.0 eV), UO_2 has low thermal conductivity and high brittleness at low temperatures.[4–6] However, at high temperatures and under irradiation UO_2 can undergo time-dependent creep.[1,4,5,7] The transition temperature from irradiation-induced[8–10] to thermal creep[11–14] is approximately 1100 °C.[4,8] Compared to the creep of metals, the creep behavior of UO_2 is much more complex, depending strongly on the O/M ratio[11,15]and, microstructural features[14,15] such as grain size and porosity, as well as temperature[4,11,14] and stress state[12,13,16]. Dozens of mechanisms have been proposed for the high temperature thermal creep. These mechanisms can be broadly classified into lattice diffusion controlled[1,11,14], grain boundary diffusion[12,17–19], and dislocation glide/climb controlled diffusion.[12–14,16] In the case of UO_2, lattice diffusion controlled creep, known as Nabarro-Herring creep, involves vacancy transport within grains, with the rate controlled by the diffusion of uranium vacancies. Dislocation controlled creep falls in two regimes: Harper-Dorn creep at low stresses and a power-law regime at high stresses. The power-law regime involves both glide and climb of dislocations. The dislocation climb rate is determined by the diffusion of vacancies to the core of the dislocation.

There is no consensus in the literature as to the dominant mechanism of thermal creep in UO_2. This can be attributed, at least in part, to the wide variability of the microstructure, stoichiometry, temperature, and presence of fission products, all of which affect the creep mechanism. To begin to re-address this complex problem in UO_2, we attempt to understand the diffusion of uranium vacancies as a function of temperature, stress state of the fuel and their interaction with the dislocations. In our simulation approach, we make use of Density Functional Theory (DFT) calculations[20–22] to accurately calculate the migration barriers of the single and di-vacancies of uranium as function of their charge state. This permits us to address uranium vacancy diffusion not only in UO_2 but also in UO_{2+x}, where, in addition to the charged vacancy (dominant in UO_2), neutral and di-vacancies are also important. Our focus is on cation vacancy diffusion as this will be the rate limiting specie controlling phenomena such as diffusion-controlled creep. We use the Kinetic Monte Carlo (KMC) method[23,24] to calculate the uranium diffusivity at relevant fuel temperatures.

This work addresses the issue of ionic transport in strained oxide materials, using UO_2 as a prototypical

material, both because of its importance in the generation of nuclear energy but also because its structure, fluorite, is common to many technologically important materials. Thus, our results have implications beyond the specific material studied, in particular for the transport properties of various systems such as complex oxide hetero-structures[25,26], strained oxide thin films[27,28], and strain enhanced ionic conductivity in fluorite structured oxide materials like CeO2 and stabilized ZrO2 (YSZ)[29–31] which are commonly used in solid oxide fuel cells, as well as sintering and creep properties of zirconia and hafnia based thermal barrier coatings[32,33]. In many of these applications, the presence of strain can alter atomic scale events and the overall evolution of the system. Importantly, as the size of these materials systems is reduced to the nanoscale and interfacial strains dominate the properties of the material, understanding the potential connection between that strain and mass transport is crucial. In addition, many other important processes that are important for a wide range of oxide ceramics involve the coupling of strain and diffusion, including sintering and creep. Finally, our work provides the foundation for an ab initio informed KMC approach and can be extended to any system where strain influences mobility.

The rest of the paper is organized as follows. In Sec.II we discuss the DFT and KMC methodologies, as well as the method to calculate the dipole tensor, which is used to address the effect of homogeneous and complex strain fields on diffusivity. We then report the migration barriers and dipole tensor values calculated for uranium vacancies using DFT (in Sec. III A and Sec. III B) as well as diffusivities for both single and di-vacancies as function of homogeneous strains and temperature in Sec. III C. Our discussion and conclusions are presented in Sec. IV.

II. METHODOLOGY

A. Density functional theory calculations

The DFT calculations are performed with the Vienna Ab Initio Simulation Package (VASP)[34–36] using the projector-augmented-wave (PAW) method.[37,38] The electron exchange and correlation potential is described by the local density approximation (LDA) with the LDA+U functional used for the correlated U 5f electrons.[39] In accordance with the earlier studies, the U and J values are set to U (4.5 eV) and J (0.51 eV); i.e., U-J (3.99 eV). Defect properties are calculated using a 2×2×3 supercell (with 144 atoms for stoichiometric UO_2). A 2×2×1 k-point mesh is used for all calculations. The supercells are allowed to fully relax, both in volume and atomic coordinates. The migration barriers are calculated using the climbing-image nudge elastic band (CI-NEB) method.[40] For each barrier we applied three, four or five nudged elastic band images, depending on the complexity of the migration path. The reported data represent the lowest energy solution which, for both stoichiometric and defect containing UO_2, corresponds to the phase with a Jahn-Teller distortion of the oxygen sub lattice.[21] Further details of the DFT calculations are presented in the work by Andersson et al.[20,21]

B. Kinetic Monte Carlo simulations

The Kinetic Monte Carlo (KMC) method[23,24] is used to simulate the long time evolution of uranium vacancies in UO_2. While molecular dynamics[41] (MD) simulations have been used to simulate uranium vacancy dynamics in UO_2[42,43], but it is limited by the accessible timescale, which is typically in the range of nanoseconds, while processes such as uranium diffusion occur on much longer time scales, even at elevated temperatures. The KMC method overcomes this time-scale limitation by exploiting the fact that the dynamics consists of advancing a uranium vacancy from one minimum energy state to the next. Thus, in principle it can take into account all diffusion pathways and the diffusion rates for each of these pathways, provided they are known. Here, these pathways and rates for uranium vacancy are calculated using DFT, which are then the input to the KMC simulations. In this work, we have employed a recently developed KMC Method[23,44] to efficiently account for arbitrary strain fields. In this method, the strain-induced changes to the migration barrier are computed using the dipole tensor approach[45–48], as described in Sec. II C. The main assumption of this technique is that the defect is in a bulk-like environment and the underlying topology of the potential energy surface does not change under relatively low strains. Under this assumption, strain serves only to change the relative heights of the stationary points on the energy surface. This is a valid assumption under small external strains, where the effect are within the linear elastic regime. The impact of strain on the pre-factor are not included as they are expected to be less important than the changes in the migration energy.[49,50] The jump rates of uranium vacancies are calculated by an Arrhenius relation as

$$k = \nu_0 \exp\left(\frac{-E_{mig}}{k_B T}\right) \tag{1}$$

where E_{mig} is the migration barrier to carry the vacancy from an initial equilibrium (or minimum of potential energy landscape) state to a saddle state, T is the absolute temperature, k_B is Boltzmann's constant and ν_0 is the migration prefactor, a measure of the entropy of migration for the process.[51] Here, E_{mig} is calculated using DFT and ν_0 from the empirical potential calculations, as described in more detail elsewhere.[21]. The values for E_{mig} and ν_0 for the two vacancy species studied in this work are listed in Table I. The diffusivity is computed from the KMC simulations using the relation between the

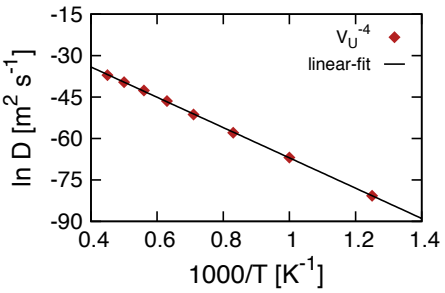

FIG. 1. Diffusivity of single charged uranium vacancy as computed from the KMC simulations. The solid line is a linear fit to the KMC data points shown in diamonds.

TABLE I. Migration parameters for a single uranium vacancy and a uranium di-vacancy. The first column gives the migration barrier (E_{mig}) in eV and second column the rate prefactor (ν_0) in sec^{-1}, taken from reference.[21]

Defect	E_{mig}	ν_0
$V_U^{\times}$	4.95	2.38×10^{12}
$V_U^{''''}$	4.72	2.38×10^{12}
$V_{U_2}^{\times}$	3.27	1.82×10^{14}
$V_{U_2}^{''''''''}$	2.84	1.82×10^{14}

mean square displacement (MSD) as function of time,

$$\left\langle R_i^2 \right\rangle = 2D_i t \tag{2}$$

where, $i \in$ [x,y,z] and the MSD, $\left\langle R_i^2 \right\rangle$ is averaged over 400 independent trajectories. The dynamics of the uranium vacancy via KMC simulations is validated by comparing it with the Arrhenius relation (Eq. 1) for the unstrained case. As expected, diffusion is isotropic ($D_X = D_Y = D_Z$) and the computed value of the diffusion coefficient for a single charged uranium vacancy $D_{V_U^{''''}}$ is 8.9×10^{-30}m^{2}sec^{-1} at 1000 K. The migration barrier (E_{mig}) and effective frequency (ν_0) calculated from the slope of the linear fit to the diffusion data are 4.72 eV and 2.39×10^{12}sec^{-1}, demonstrating the correctness of the KMC implementation, which are same as the input values of 4.72 eV and 2.38×10^{12}sec^{-1}, demonstrating the correctness of the KMC implementations. E_{mig} is extracted from the KMC simulation from the slip of $ln[D = D_0 exp(-E_{\mathrm{mig}}/k_B T)]$ vs inverse temperature while ν_0 is found from the relationship $D_0 = \frac{1}{6} f Z S^2 \nu_0$, where $f = 1$, $Z = 12$ and $S = 0.386$nm.

C. Dipole tensor formalism

Point defects can introduce lattice distortions both at short and long range. The short range distortions consist of relatively large displacements of ions in the immediate neighborhood of the defect, whereas long range distortions can be understood from linear elasticity theory.[46,47,52] A point defect or the lattice distortion associated with it interacts with external strains, which induces a change in the defect's energy of formation. This change in energy due to external strain can be described, to first order, by the elastic dipole tensor.[45–47,53,54] The change in energy is given by

$$\Delta E = -tr(\boldsymbol{G} \cdot \boldsymbol{\varepsilon}) = -G_{ij}\varepsilon_{ij} \tag{3}$$

where ΔE is the change in the energy of formation of the defect between the strained and unstrained environments. G_{ij} is the second-rank elastic dipole tensor and ε_{ij} is the external strain tensor. G_{ij} and ε_{ij} are symmetric tensors and the right hand side of Eq.3 is shown in Einstein summation convention. Note that, from the definition of **G**, it is a property of the defect, has units of energy (eV) and, in the linear elastic regime, is independent of the externally applied strain. Techniques to compute the elastic dipole tensor **G** were first developed in the mid-1950s, and can be broadly grouped into three methods: the Kanzaki-Hardy force method[54,55], Gillan's strain derivative method[46,47], and the stress/strain-based method[48,56]. In the present work, we have used the stress/strain-based method, since it is computationally less expensive than the others, requiring only the examination of a single defect configuration. Gillan's strain derivative method involves calculation of the energy of formation of the defect at different strain states and computing the derivative of the energy with respect to the strain. The Kanzaki-Hardy force method on the other hand, as discussed in literature[46,47] can be difficult to apply, especially for more complex defect structures. Gillan's and stress/strain methods have been shown to be more accurate than Kanzaki-Hardy force method.[46,48] For the purpose of verification we have tested the Gillan and stress/strain method for the simpler case of a vacancy in Zr and found the calculated dipole tensor to be very close to the other reported values.[23]

The calculation of the dipole tensor **G** from the stress/strain-based method is quite straightforward and can easily be applied to the common supercell approach uses in atomistic and electronic-structure calculations for impurities and point defects. Point defect calculations based on DFT can be carried out in two ways. One way of introducing the defect is by keeping the supercell size and shape fixed with respect to the bulk (defect free) structure ($\varepsilon_{ij} = 0$) and allowing only for relaxations of atomic positions. We will refer to this as constant volume of strain-controlled approach. In this approach a simulation box containing a defect will develop a finite stress σ_{ij}, which gives the measure of the dipole tensor **G** for the point defect. Alternatively, atomic simulation can be done where supercell size, shape and atomic coordinates are allowed to relax to zero stress ($\sigma_{ij} = 0$). This is the constant pressure or stress-controlled approach, where the simulation box containing the defect will develop a finite strain ε_{ij}, measured with reference to the equilibrium bulk (defect free) structure. The general expression

to calculate the dipole tensor **G** from the stress/strain-based method has been derived in the literature[48,56] and is given by

$$G_{ij} = V(C_{ijkl}\varepsilon_{kl} + \sigma_{ij}) \tag{4}$$

where V is the volume of the simulation cell containing the point defect, C_{ijkl} is the elastic constant tensor, σ_{ij} and ε_{ij} are the stress and strain tensor of the defect structure as mentioned in the discussion above. The elastic constants[57] used in Eq. 4 are those of the perfect (defect free) bulk UO_2. The difference in elastic constants between the defect and perfect structure[58–60] can have an effect on the dipole tensor calculations, but in our simulations we find this to be negligible. Calculation for the dipole tensor via both stress and strain controlled approaches, as discussed next, show very good agreement. Further, after evaluating the energy vs. volume curves (which are related to the elastic constants) for both the perfect and defect structures, we find both curvature to be very close. It is thus reasonable to assume that the elastic constant C_{ijkl} do not change much from the bulk value for the studied concentration of defects and small-applied strains. For the strain-controlled limit ($\varepsilon = 0$), Eq. 4 reduces to

$$G_{ij} = V_0\sigma_{ij} \tag{5}$$

where V_0 is the volume of simulation cell containing the point defect, which is the same as the volume of the perfect-crystal structure. σ_{ij} is the stress of the defect simulation cell calculated from atomistic calculations. In the stress-controlled limit ($\sigma = 0$), Eq. 4 reduces to

$$G_{ij} = VC_{ijkl}\varepsilon_{kl} \tag{6}$$

where ε_{kl} is the strain of the relaxed defect simulation cell (with volume V) with respect to the bulk simulation cell. Once we know the elastic dipole tensor **G** for the defect in a given configuration, we can calculate the change in defect energy ΔE due to strain using Eq. 3 and use this to recompute the migration barrier E_{mig} is defined as

$$E_{mig} = E_{saddle} - E_{minimium} \tag{7}$$

where E_{saddle} and $E_{minimum}$ are the energy of the migration ion at the saddle point and the equilibrium minimum site, respectively. Under the external strain, E_{mig} will be modified due to changes in both E_{saddle} and $E_{minimum}$ as

$$\begin{aligned} E_{mig}^{strained} &= [E_{saddle} + \Delta E_{saddle}] - [E_{min} + \Delta E_{min}] \\ &= E_{mig} + \Delta E_{mig}^{strained} \end{aligned} \tag{8}$$

$$E_{mig}^{strained} = \big[E_{saddle} - E_{min}\big] - \Big(G_{ij}^{saddle}\varepsilon_{ij} - G_{ij}^{min}\varepsilon_{ij}\Big) \tag{9}$$

$$\begin{aligned} E_{mig}^{strained} &= \big[E_{saddle} - E_{min}\big] - \Big((G_{ij}^{saddle} - G_{ij}^{min})\varepsilon_{ij}\Big) \\ &= \big[E_{saddle} - E_{min}\big] - \Big(\Delta G_{ij}^{mig}\varepsilon_{ij}\Big) \end{aligned} \tag{10}$$

where the ΔE are given by Eq.3 for the saddle and the minimum, respectively and $\Delta E_{\rm mig} = \Delta E_{\rm saddle}$ - $\Delta E_{\rm min}$ is the measure of change in migration barrier due to strain. Thus, the dipole tensor **G** must be calculated for both the saddle and the minimum energy structure to estimate the change in the migration energy. Expanding Eq. 8 using the definition of the dipole tensor from Eq. 3, we can write Eq. 9. Note that the strain ε_{ij} may not always be same at the saddle and minimum site; for example in the case of a dislocation, the strain field varies with the distance from the dislocation core. However, under homogeneous external strains such a uniaxial tensile, compression or shear, the strain ε_{ij} will be same at both the saddle and the minimum, and therefore, Eq. 9 can be further simplified in Eq. 10 and hence, using Eq. 8 we can define $\Delta E_{\rm mig}$ as change in the migration barrier under homogeneous external strains as

$$\Delta E_{mig}^{strained} = -tr(\boldsymbol{\Delta G^{mig}} \cdot \boldsymbol{\varepsilon}) \tag{11}$$

The elastic response of both the minimum and saddle to external strain is then completely embedded in $\Delta G_{ij}^{\rm mig} = G_{ij}^{\rm saddle} - G_{ij}^{\rm min}$. This is an important relation, as it shows that the change in migration barrier $\Delta E_{\rm mig}$ depends on the dipole tensor of the saddle state with respect to the minimum state, i.e. to the difference ΔG_{ij} under homogeneous strains, and not on the individual dipole tensors of the saddle and minimum. This is in line with the recent study by Hinterberg et al.[61] who employ an activation volume tensor $\Delta V_{\rm mig}$ approach to study the effect of different homogeneous strain states (uniaxial, biaxial and isotropic) on oxygen vacancy diffusion. In their approach, the modified migration barrier $\Delta H_{\rm mig}$ changes is an external strain field by -tr($\sigma \cdot \Delta V_{mig}$) where σ is the externally applied stress tensor and $\Delta V_{\rm mig}$ the activation volume tensor of the defect. The elements of the tensor $\Delta V_{\rm mig,kl}$ are calculated for the saddle state with respect to the initial state.

III. RESULTS

Using barriers and pre-factors computed using DFT and empirical potentials, respectively, we parameterize a KMC model that uses rates modified by imposed strains as calculated via dipole tensor formalism. We first describe the detailed pathway for uranium vacancy migration and then results on the computed diffusivity of both single vacancies and uranium di-vacancies using the KMC model under homogeneous external strains. Various strain states have been considered: uniaxial and shear strains (up to $\pm$ 2% in all cases). We also performed calculations for biaxial and isotropic strains, but the results were qualitatively similar to these cases so

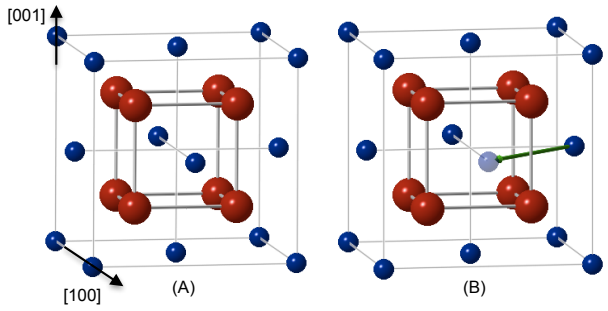

FIG. 2. (A) UO_2 unit cell. Uranium (small/blue) ions are arranged in an FCC lattice; oxygen (large/red) ions occupy tetrahedral sites forming a simple cubic lattice. (B) Shows a vacancy at a uranium site (small/gray) and a possible hop to a neighboring uranium site along a ⟨110⟩ direction type.

they are not further considered. The diffusivities are found to be highly sensitive to the applied strain and, as expected, on the vacancy type (single or di-vacancy). The response of the single and di-vacancy diffusion to strain is very different and is discussed in detail in the next sections.

A. Migration paths and energy barriers

Uranium dioxide (UO_2) has a fluorite crystal structure as shown in Figure 2 with U^{4+} ions forming a FCC lattice and O^{2-} ions occupying all eight tetrahedral sites, thereby forming a simple cubic lattice. The space group of fluorite crystal structure is $Fm\bar{3}m$ (number 225) with cations occupying the 4a Wyckoff sites while anions occupy 8b sites. The migration energies for uranium self-diffusion in non-stoichiometric as well as stoichiometric UO_2 have been studied experimentally.[62–65] However, a detailed exploration of the defect energies, energy barriers and uranium migration paths has only been made possible recently by first-principles based density functional theory (DFT) calculations.[20–22,66–68] In this study, we use the work of Andersson et al.[21] in which various charged single uranium vacancies and their clusters have been studied for UO_{2-x}, UO_2 and UO_{2+x}, both for intrinsic and irradiation conditions. For stoichiometric UO_2, the fully charged uranium vacancy ($V_U^{''''}$) is the thermodynamically stable defect[20,66,69] and hence control uranium diffusion. For UO_{2+x}, and under irradiation conditions, clusters of two uranium vacancies can be present and can contribute significantly to transport as they have lower migration barrier than the single uranium vacancies.

The diffusion mechanism of a uranium ion involves migration from its equilibrium lattice site (minimum) to its nearest uranium vacancy site along ⟨110⟩ type directions, as shown schematically in Figure 2. This involves significant displacement of oxygen ions close to the migration path of the uranium ion.[22] The migration of the uranium vacancy follows a curved path between the vacancy and its nearest neighbor rather than the direct path along the ⟨110⟩direction, i.e., the uranium vacancy passes close to an empty octahedral position in the unit cell, as shown in Figure 3. A similar curved path for oxygen diffusion in perovskite-type oxides[70] as well as in δ-Bi_2O_3, whose structure is related to the fluorite structure, has been seen experimentally[71] and discussed in atomic simulations.[72] At the saddle point, the two nearest oxygen ions are significantly displaced to make way for the migrating uranium ion and the saddle point is not located halfway between the initial and final positions. Instead, Andersson et al.[20,21] observed a two-saddle pathway for a migrating uranium vacancy forming a split vacancy structure (Figure 3) between the two saddles, corresponding to a shallow minimum at the mid-way point along the path. A schematic of the energy landscape is shown in Figure 4. Further, the migration path of the uranium ion from one lattice site to another is tilted by a small angle of about 1.2 degrees from the (001) plane (dotted line in Figure 5). Hence, as shown in Figure 5, due to the curved migration path and the 2-fold symmetry along the ⟨110⟩ direction, migration of the uranium ion can occur via a total of four symmetric paths for a given ⟨110⟩ direction.

B. Dipole tensor calculations

1. *Single uranium vacancy*

An ideal cation vacancy in the fluorite structure has cubic symmetry, as it can be visualized as residing at a center of the cube formed by the first eight neighboring oxygen ions. As discussed by Leslie[52] and Freedman[56] the dipole tensor for a defect in an ideal cubic symmetry has only diagonal elements. However, the symmetry of a cation lattice in UO_2 may actually deviate from ideal cubic symmetry due to Jan-Teller distortion of the oxygen sub-lattice at low temperature, by lowering the symmetry as well as the energy of the system.[20,73,74] This Jahn-Teller distortion is directly linked to the orientation of the magnetic moment of uranium ions.[73,75,76] In our calculations, 1k antiferromagnetic (AFM) ordering is employed, as it has been argued that 1k AFM order is closer to the actual paramagnetic state at high temperature, and is shown to be a good approximation for defect energies.[20,77] Consistent with this, DFT+U calculations of UO_2 show deviations from cubic symmetry for uranium vacancy and, therefore we observe off-diagonal elements for dipole tensor compared to relatively large diagonal components. In this study, we have investigated two extreme charge states for vacancies and di-vacancies: neutral and fully charged. The calculated dipole tensor (in eV) of a neutral uranium vacancy ($V_U^{\times}$) and the saddle point along the curved path along the ⟨110⟩ direction

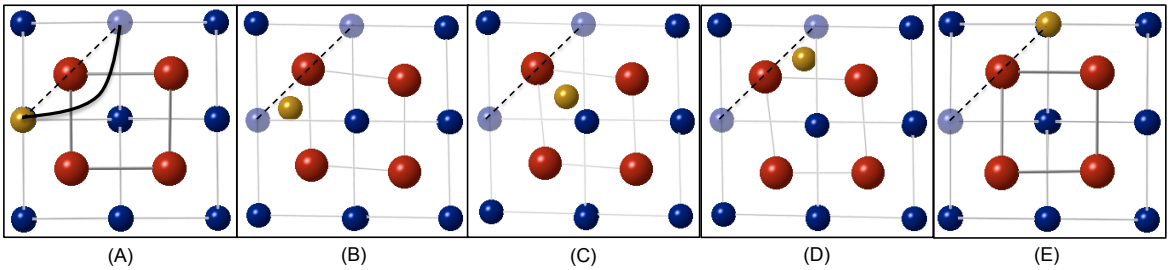

FIG. 3. Snapshots of uranium vacancy migrating to its nearest neighbor position along the ⟨110⟩ direction, as predicted from the DFT calculations. The migrating uranium ion is shown in yellow, the dashed black line represents the straight path along ⟨110⟩ direction, whereas the black curve traces the actual path (curvature exaggerated for visualization). The vacancies are indicated in gray. (C) shows the metastable intermediate minimum along the migration path, as described in Figure 4.

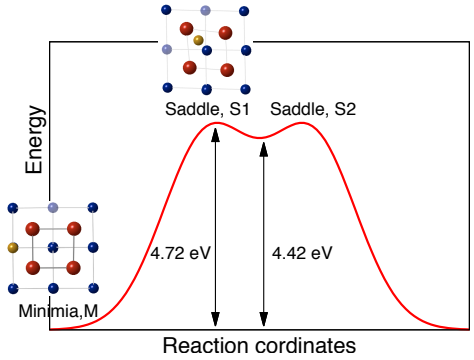

FIG. 4. Schematic of the energy vs. the migration path for the uranium vacancy, showing an intermediate shallow minimum, corresponding to the migrating ion residing close to an interstitial site and forming a split vacancy structure.

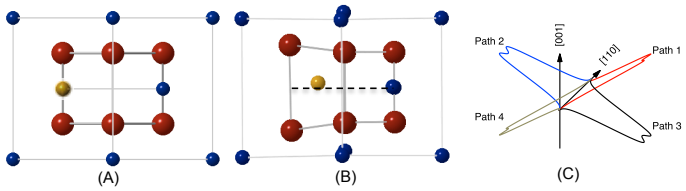

FIG. 5. (A) Two-fold rotation symmetry along the ⟨110⟩ direction in the fluorite structure; (B) Saddle structure with the migrating uranium ion slightly off (angle 1.2 degrees) the (001) plane, as marked by dashed lines; (C) Schematic of all four reconstructed paths along ⟨110⟩ direction; the angle between the different planes of migration is exaggerated for clarity.

are

$$G^{min}_{V_U^\times} = \begin{bmatrix} -10.83 & -0.14 & 2.06 \\ -0.14 & -17.10 & -1.46 \\ 3.06 & -1.46 & -9.35 \end{bmatrix} eV$$

$$G^{saddle}_{V_U^\times} = \begin{bmatrix} 13.29 & -2.18 & -1.80 \\ -2.18 & -1.50 & 11.76 \\ -1.80 & 11.76 & 1.72 \end{bmatrix} eV$$

We note that, in contrast to the dipole tensor for the minimum, there is no constraint that dipole tensor of the saddle point has to be diagonal, even in the cubic crystal, as it does not have to retain the cubic symmetric of the crystal. The negative diagonal components of the dipole tensor for the minimum state express the tendency of the crystal to contract due to the presence of a uranium vacancy ($V_U^\times$). A major part of this contraction comes from the U^{5+} ions present in the neutral supercell that form spontaneously to compensate for the missing electrons due to the missing uranium ion. Also, we notice that the largest element of the dipole tensor of the minimum coincides with the direction of the plane containing the highest concentration of U^{5+} ions. To account for diffusion of the uranium vacancy in the KMC simulations, we need to consider all possible paths of a single uranium vacancy to its twelve nearest neighboring sites, each lying along a different but equivalent ⟨110⟩ direction. Since the path to a single neighboring uranium ion has four-fold degeneracy (Figure 5), and given a uranium vacancy has twelve nearest neighbor uranium atoms in fluorite structure, it has a total of forty-eight unique paths by which it can hop from one uranium site to another. Further, because each path is comprised of two saddles and an intermediate minimum, there are ninety-six saddles that represent the hop of one uranium vacancy to a nearest neighbor site in UO_2. As discussed in Sec. II, the change in migration barrier due to homogeneous strain depends only on the relative dipole tensor $\Delta G^{\text{mig}}_{ij}$ of the saddle with respect to the minimum. In Table II, we report $\Delta G^{\text{mig}}_{ij}$ for the fully charged and neutral uranium vacancy. The reported dipole tensors are for one particular direction (i.e. [110]); dipole tensors for the remaining forty-seven paths are calculated by applying tensor operations that account for crystal and path symmetry, as discussed in the appendix.

2. *Uranium di-vacancy*

A single uranium vacancy can form a di-vacancy with another uranium vacancy present at any of its twelve

TABLE II. Calculated ΔG_{ij} (in eV) for charged and neutral single uranium vacancy

Dipole tensor	ΔG_{11}	ΔG_{22}	ΔG_{33}	ΔG_{12}	ΔG_{13}	ΔG_{23}
$\Delta G_{V_U^{''''}}$	24.67	11.13	12.04	−0.16	−0.16	7.53
$\Delta G_{V_U^{\times}}$	24.12	15.61	11.07	−2.03	−4.86	13.22

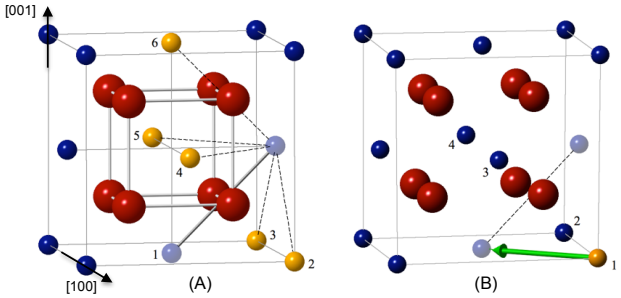

FIG. 6. (A) The six distinct di-vacancy configurations within first nearest neighbors in UO_2 unit cell, all other possibilities would be a simple translation of the above six configurations. (B) The four possible sites a single di-vacancy can hop to in order to maintain a di-vacancy pair.

nearest neighboring sites along ⟨110⟩ type direction. However, only six of these are distinct orientations. For example a uranium vacancy at (0,0,0) can for a di-vacancy configuration with neighboring uranium sites at $\left(\frac{1}{2},\frac{1}{2},0\right)$, $\left(\frac{1}{2},-\frac{1}{2},0\right)$, $\left(0,\frac{1}{2},\frac{1}{2}\right)$, $\left(0,-\frac{1}{2},\frac{1}{2}\right)$, $\left(\frac{1}{2},0,\frac{1}{2}\right)$, $\left(\frac{1}{2},0,-\frac{1}{2}\right)$, as shown in Figure 6. The dipole tensor for a uranium di-vacancy oriented along [110] is given as

$$G^{min}_{V^{\times}_{U_2}} = \begin{bmatrix} -24.25 & 5.47 & -1.50 \\ 5.47 & -24.82 & -2.09 \\ -1.50 & -2.09 & -24.79 \end{bmatrix} eV$$

Migration of the uranium di-vacancy can be understood in terms of migration of one of its constituent vacancies[21], with one vacancy fixed at its lattice site and other vacancy hopping to the nearest uranium site (Figure 7). In order to preserve the low energy ($V_U^{\times}$–$V_U^{\times}$) pairing (binding energy[21] of -0.01 eV and -0.30 eV for $V_U^{''''}$–$V_U^{''''}$ pair), a migrating vacancy comprising the di-vacancy complex is constrained to move to one of the four nearest di-uranium vacancy sites (Figure 6), because the site to which it migrates should be a nearest neighbor to both the migrating vacancy and to the non-migrating vacancy. Either vacancy in the di-vacancy cluster can hop to one of its four nearest neighboring sites via two distinct paths, therefore for a di-vacancy there are sixteen possible paths (2 vacancies × 2 path per vacancy × 4 neighboring states) to hop from one state to another instead of the forty-eight paths for a single vacancy.(Note that, in contrast to the mono-vacancy in which there are four paths for each hop direction, there are only two for the di-vacancy due to the presence of the second vacancy). However, the overall KMC catalog for the di-vacancy is much more

TABLE III. Calculated ΔG_{ij} (in eV) for charged and neutral uranium di-vacancy

Dipole tensor	ΔG_{11}	ΔG_{22}	ΔG_{33}	ΔG_{12}	ΔG_{13}	ΔG_{23}
$\Delta G_{V_{U_2}^{''''''}}$	10.86	9.73	−4.80	−0.76	−4.67	4.04
$\Delta G_{V^{\times}_{U_2}}$	13.05	15.33	−3.75	−0.96	−3.83	4.91

complex, as there are six distinct di-vacancy states; thus we have in total ninety-six paths with two saddles per path. The migration path is similar to that of a single vacancy as discussed in Sec. III A, which is a curved path along ⟨110⟩ direction consisting of two saddles (shown in Figure 7). As mentioned, a di-vacancy has sixteen possible migration paths and to account for dipole tensor for all the saddles, we applied tensor operations as per the symmetry of the system. The dipole tensor for a saddle specific to migration path along [110] is given as

$$G^{saddle}_{V^{\times}_{U_2}} = \begin{bmatrix} -11.19 & 4.51 & -5.33 \\ 4.51 & -9.49 & 2.82 \\ -5.33 & 2.82 & -28.54 \end{bmatrix} eV$$

C. Homogeneous strains

The strain state of the fuel pellet in operation can be very complex, as it depends on factors such as the temperature distribution, presence of fission products, changes in microstructure, and pellet-clad interaction.[1] Nevertheless, simple strain states such as uniaxial tension, compression and shear can provide useful insight into the much more complex problem. Here we report the effect of homogenous strain states (uniaxial and shear) on the diffusion rate of uranium single and di-vacancies. KMC simulations based on the dipole tensor approach are used to calculate diffusion rates, as they explicitly incorporate the effect of strain on all paths (48 paths for single vacancy and 96 paths for six distinct di-vacancy states) as well as their saddles.

1. *Single uranium vacancy*

Both neutral and charged point defects in uranium dioxide have been studied.[20,21,66,67] Charged defects are thermodynamically more favorable in stoichiometric UO_2; however neutral defects may be favored under non-stoichiometric conditions, more specifically in $UO_{2+\times}$ for which the Fermi level is close to the valence band edge. In this work, we have investigated the diffusivity of both fully charge and neutral defects. We first report the change in migration barrier ΔE_{mig} from Eq. 11 using the dipole tensor $\Delta G^{\text{mig}}_{ij}$ as listed for single vacancies in Table II, followed by diffusion coefficients as a function of temperature as well as strain state. E_{mig} and

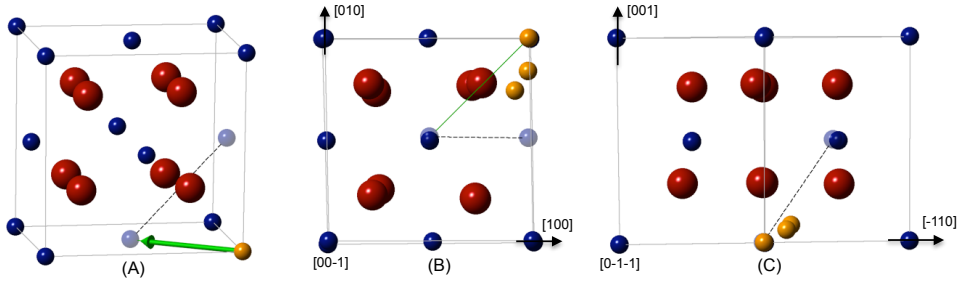

FIG. 7. (A) Schematic showing that the migration of a uranium di-vacancy (dashed line) is related to the migration of one of its constituent vacancies. (B) Combined snapshots of the migrating uranium ion (shown in yellow in Fig. 7A) to the nearest vacancy along ⟨110⟩ direction, as determined from the DFT calculations. The green solid line represents straight path along ⟨110⟩, but from the snapshots it is clear that the path is curved away from the ⟨110⟩ direction as well as tilted (Fig. 7C) from the (001) plane, similarly to the behavior for the single vacancy as discussed in the text.

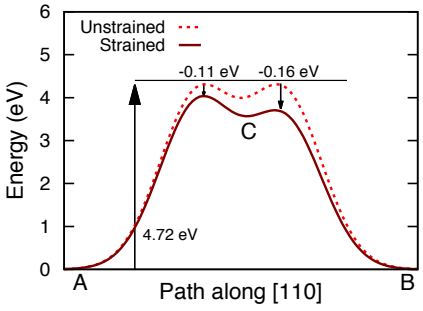

FIG. 8. Schematic showing the change in migration (transition from A to B) for one of the paths oriented along [110] for an applied tensile strain of 1% along [100] for $V_U^{\times}$. The dotted red curve corresponds to the unstrained energy barriers. The red solid curve shows the change in energy barrier for both saddles to an 1% applied tensile strain.

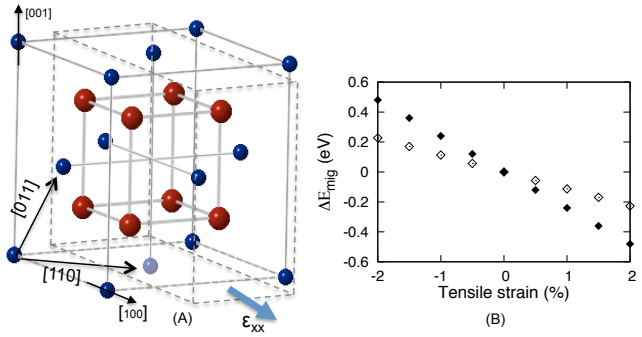

FIG. 9. (A) Schematic showing the applied strain along the [100] direction with the black arrows points towards the uranium vacancy possible migrations along the [110] and [011] directions. (B) Change in the migration barrier $\Delta E_{\rm mig}$ for $V_U^{\times}$ under applied uniaxial tensile strain along [100] for migration path oriented along [110] (open diamonds) and [011] directions (solid diamonds).

ν_0 values for the unstrained case are listed in Table I. In our calculations, we make the approximation that the effect of strain on diffusivity is primarily due to change in $E_{\rm mig}$ and ν_0 is kept constant. We computed $\Delta E_{\rm mig}$ for both neutral and fully charged vacancies under uniaxial strain to measure if they respond differently to the applied strain. Figure 8 shows the change in migration barrier $\Delta E_{\rm mig}$ for a neutral vacancy, for a specific path in the [110] direction under the uniaxial tensile strain of 1% along the [100] direction. A uniaxial tensile strain decreases the energy barriers compared to the unstrained case (as $\Delta E_{\rm mig}<0$) for both saddles along a given path (Figure 8 solid red curve)) and hence , a [100] tensile strain will increase the diffusion rate along [110]. The energy of the two saddles changes by different magnitudes to the applied 1% tensile strain with the energy of one saddle decreasing by 0.16 eV and that of the other by 0.11 eV. In the KMC simulations, the change in barrier height for both the saddles due to strain are calculated, but only the higher of the two barrier is used in KMC simulations to calculate the diffusion rate from site A to B. This is justified because the minimum at state C is very shallow (with depth of only 0.3 eV and 0.8 eV for the single and di-vacancy, respectively) especially compared to the unstrained barrier of 4.72 eV and even to the changes in barrier height of 0.16 and 0.11 eV due to strain. Therefore, the true trajectory would not thermalize in the shallow state at temperatures where the 4.72 eV barrier can be overcome and it is appropriate to not explicitly consider it in the KMC rate catalog. Hence, our KMC model selects the higher of the two barriers after explicitly calculating the change in barrier height for the both of the saddles under strain. For a uniaxial strain along [100], the change in barrier energy along each of the four [110] paths is effectively same (-0.11 eV), though which of the two saddles change more in energy depends on the details of the path. Further, we have determined the change in migration barrier $\Delta E_{\rm mig}$ as a function of the orientation of the path relative to the strain. Figure 9 schematically illustrates the relative orientation of two different paths to a tensile strain in the [100] direc-

tion, and the change in migration energy barriers along the [110] and [011] directions in response to an externally applied tensile strain along [100]. Directions, which are normal to the applied strain i.e. of ⟨011⟩ type, respond differently than the ⟨110⟩ and ⟨101⟩ families of directions, which have some component of applied strain parallel to them. This asymmetry in the diffusion is expected because the tensile strain along [100] will affect the paths in (001) plane and normal to the (001) plane differently. In the first case, there is a component of strain along the pathway, which is not so in the second case. In Figure 10, the relative diffusivities of charged uranium vacancies are calculated at 1800 K, which is a reasonable temperature for an intrinsic diffusion within the fuel; these are plotted as function of temperature in Figure 11. A uniaxial strain along [100], enhances the diffusivities in all the there cubic directions [100], [010] and [001] with $D_{[100]} \neq D_{[010]} \sim D_{[001]}$. This is anticipated, as a uniaxial strain will change the ideal cubic symmetry of the unstrained fluorite structure to tetragonal symmetry. We also note that ΔE_{mig} is negative and positive for the tensile and compressive strains, respectively for both of the charge states of the single vacancy, and the magnitude of increase in diffusivity under tension is greater than the reduction under the compressive strain of same order. This is expected given the exponential dependence of diffusion rate to the change in migration barrier (Eq. 1) and similar observations has also been observed in simulations on strained fluorite-structured CeO_2.[78] The relative diffusivity is found to be less sensitive to the charge state of the single vacancy, when subjected to the same uniaxial strain state (as shown in Figure 14). We next analyze the effect of shear strain on diffusivity. A fuel pellet can develop shears strain along with the normal components during initial synthesis processes such as hot pressing.[79] Moreover, under operation conditions within the reactor, the stress state on the fuel pellet can be quite complex. Therefore it is relevant to characterize the effect of shear strain on diffusivity, in particular to understand the diffusion as its related to sintering processes. The computed ΔE_{mig} shows that the shear strain decreases the migration barrier more significantly for paths oriented in plane of shear as compared to paths oriented normal to it. Figure 13 shows that the overall diffusivity increases with increasing shear strain, with relative increase being more prominent at lower temperature. Comparing the diffusion coefficients of neutral and charged vacancies under the same shear strain states, we find that their behavior is significantly different. Under a shear strain along ⟨110⟩ the diffusivity of the neutral vacancy increase by the factor of two more than that of the charged vacancy (Figure 14). This is a significant difference, even at temperature as high as 1800 K.

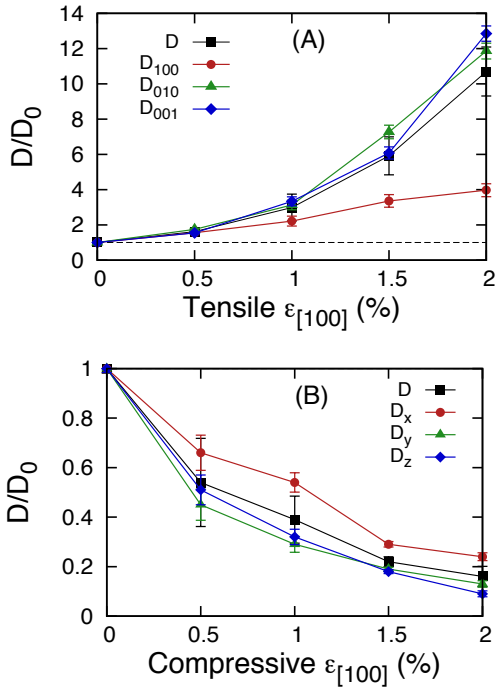

FIG. 10. Relative diffusivity of the fully charged uranium vacancy ($V_U^{''''}$) under (A) tensile and (B) compressive strains at 1800 K. D_0 corresponds to the diffusivity under no external strain. Red, green and blue curves, represent relative diffusivities along the [100], [010] and [001] directions, respectively and the black curve represents the overall relative diffusivity.

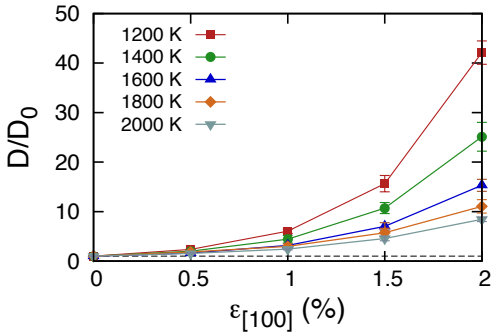

FIG. 11. Relative diffusivity of the fully charged uranium vacancy ($V_U^{''''}$) as a function of temperature under uniaxial tensile strain. D_0 corresponds to the diffusivity at each temperature under no external strain.

2. *Uranium di-vacancy*

In UO_{2+x} (i.e. in an oxidizing environment) and under irradiation conditions, the uranium di-vacancy can be an important defect due to its higher overall concentration, as suggested by Andersson et al.[21] DFT calculations predict that the di-vacancies have low migration barrier compared to that of the single uranium vacancy

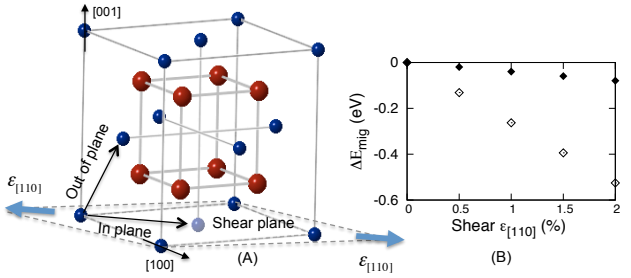

FIG. 12. (A) Schematic showing the applied shear strain in the (001) plane along with the black arrows indicating the in-plane and out-of-plane (relative to the applied shear) migration pathways of the uranium vacancy. (B) Change in migration barrier ΔE_{mig} for ($V_U^{''''}$) under the applied shear strain for paths oriented in plane (open diamonds) and normal (solid diamonds) to the shear plane.

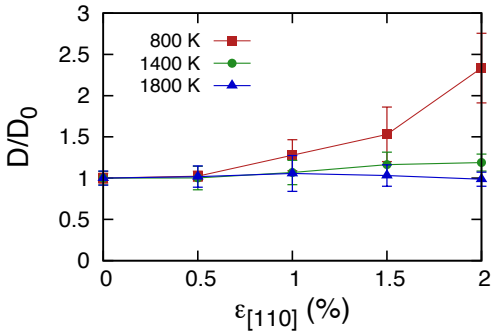

FIG. 13. Relative diffusivity of the full charged uranium vacancy ($V_U^{''''}$) as a function of temperature under shear strain.

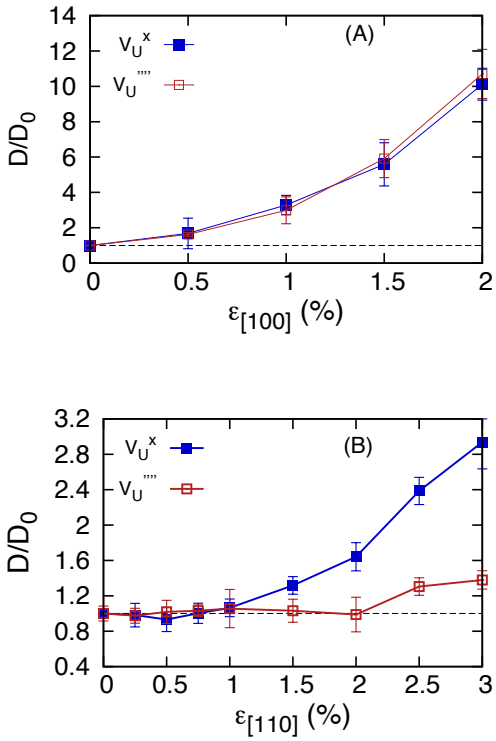

FIG. 14. Comparison of diffusivities of neutral and charge uranium vacancies, (A) under a uniaxial strain along the [100] and (B) shear strain along the [110] at 1400K.

(see Table I) and can thus increase the overall uranium diffusivity, even if they are only present in small concentrations. The difference in response to uniaxial and shear strain between the single vacancy and the di-vacancy is due to the difference in the dipole tensor $\Delta G_{ij}^{\text{mig}}$ for the two defects. The magnitude of the diagonal and some of the off-diagonal elements of the dipole tensor for the di-vacancy are smaller than for the single vacancy (Table III). However, it is not just the magnitude but also the sign of the elements of the dipole tensor that determines the overall change in diffusivity. One clear difference between the two defects is in the response to shear strain. For a single vacancy, shear strain significantly increases the in-plane diffusivity but only increases the out-of-plane relative diffusivity by a small amount (Figure 12). However, the di-vacancy has both lower out-of-plane and in-plane relative diffusivities because of its positive and negative off-diagonal elements, which can couple with specific orientations of shear strains. The calculated diffusivity for the neutral uranium di-vacancy as a function of strain and temperature are presented in Figure 15. As expected, the effect of strain is substantial at relatively low temperatures, less than 1200 K, at which U diffusion is slow. A neutral di-vacancy is found to interact more strongly with the external uniaxial strain, as the increase in its diffusivity is about three times more than that for a charged di-vacancy (Figure 15). For a uniaxial strain along $\langle 100 \rangle$, we find that the diffusion rates for a neutral di-vacancy (Figure 15) follows a trend $D_{\langle 100 \rangle} < D_{\langle 010 \rangle} \sim D_{\langle 100 \rangle}$. For a shear strain, we see a small decrease in overall diffusivity for strains up to 1% and then an increase for higher shear strains (Figure 15), for both neutral and charged di-vacancy.

IV. DISCUSSION AND CONCLUSIONS

The diffusivities of a single uranium vacancy and a di-vacancy were studied as a function of external homogeneous strain, temperature and charge state of the defect. We reported curved migration paths and non-cubic symmetry for the uranium vacancy. This is different from the straight migration paths and cubic symmetry of an ideal cation vacancy in the fluorite structure. A dipole tensor approach was used to calculate the change in migration barrier due to external strains. We have shown (Eq. 11) that under homogeneous strain fields, only the dipole tensor of the saddle with respect to the minimum i.e. $\Delta G_{ij}^{\text{mig}} = G_{ij}^{saddle} - G_{ij}^{min}$ is required to correctly calculate the change in energy barrier ΔE_{mig} between the

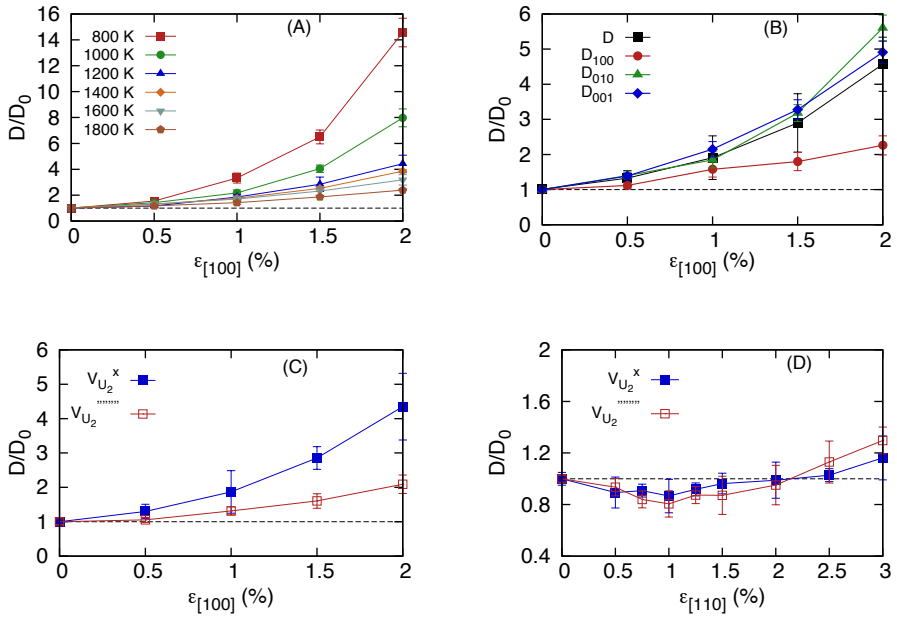

FIG. 15. (A) Relative diffusivity of the neutral di-vacancy under tensile strain as function of temperature. D represents the calculated diffusivity under strain, and D_0 is the diffusivity at zero strain at same temperature. (B) Relative diffusivity of neutral di-vacancy ($V^{\times}_{U_2}$) at 1400 K under tensile strain along [100]. Relative diffusivities along [100], [010] and [001] directions are shown via the red, green and blue curves, respectively and the overall diffusivity by black curve. (C) and (D) compare the diffusivity of charged and neutral di-vacancies under tensile and shear strains, respectively.

strained and the unstrained case. Table IV compares the effect of strain for different types of applied strain on the four different defect structures considered in this manuscript. As is evident from the table, the changes in relative diffusivity are less sensitive to the charge of the defect than the size of the defect. Further, single vacancies are more sensitive to all nature of applied strain than di-vacancies. This has important implications for the evolution of the fuel, particularly thermal creep and sintering. During sintering, a thermal process, the majority of the vacancies will be single vacancies. The diffusivity of these defects is particularly sensitive to the strain state and thus the sintering kinetics will be sensitive to the detailed microstructure of the material. In contrast, irradiation induced creep will be controlled, to a greater extent, by the kinetics of di-vacancies which does not vary as significantly with strain. Thus, to first order, creep rates in the irradiated fuel will be less sensitive to the overall strain state of the fuel. These conclusions imply that it is more critical to understand the strain state for predicting sintering under thermal conditions than it is for predicting creep in irradiated fuel.

More generally, the strain-induced anisotropy of point defect diffusion should be taken into account in calculating the defect fluxes to sinks like dislocations, cavities etc., as accurate evaluation of the sink absorption efficiency for point defects is critical in determining creep rates[80]. Sinks create an elastic strain field in their vicinity, which will lead to anisotropic diffusion of point defects and therefore a biased flux of point defects to those sinks. Hence, understanding diffusion rates as a function of major crystal directions as well defect type like vacancies, interstitials etc., is important in calculating creep rates, swelling behavior, and dislocation substructures etc.[81,82] In our results (Figure 10 and Figure 15) we show diffusivities of single and di-uranium vacancies as function of major crystal directions ⟨100⟩, ⟨010⟩ and ⟨001⟩ under a homogeneous uniaxial strain along ⟨100⟩ and report that the diffusion along ⟨010⟩ and ⟨001⟩ is more favored compared to diffusion along ⟨100⟩. That is, the strains couple with defect diffusion in complex ways, with strains along one direction significantly influencing diffusion in perpendicular directions. These anisotropies mean that, in the complex strain fields associated with dislocations, the flux of defects to the dislocations will be quite convoluted, in contrast to the assumptions made by simple cylinder models of defect fluxes to dislocations.[83] For example, while the strain fields of edge dislocations indicate that defects and fission products will be attracted to the core[84,85], the coupling with the dipole tensors suggests that greater enhancements in diffusion might occur along the edge dislocation line rather than toward the core (perpendicular to the line direction). These insights have important implications in understanding fuel creep and point to the need of comprehensive models that account for these anisotropies.

This dipole tensor approach can easily be extended to measure the effect of any arbitrary strain state on dif-

TABLE IV. Summary of the relative diffusivities D/D_0, where D_0 is the diffusivity at 0% strain, for different strain states for the four defects considered here, at a strain of 2% and temperature of T=1800 K.

Defect	Tensile $\epsilon_{[100]}$	Compressive $\epsilon_{[100]}$	Shear $\epsilon_{[110]}$
$V_U^{\times}$	10.12	0.11	1.64
$V_U^{''''}$	10.7	0.16	0.99
$V_{U_2}^{\times}$	2.97	0.24	1.03
$V_{U_2}^{''''''''}$	1.87	0.42	0.92

fusivity, as long as the applied strains are small enough to not change the migration topology of the defect. In this work, applied strains were within 2%. During operation, the thermal gradients that develop within the fuel can easily lead to such magnitudes of strain.[1,86–88] We found that strain has a significant effect on the diffusivity, especially at low temperatures, with compressive strain leading to lower diffusivity and tensile strain to higher diffusivity. The diffusivity of a single uranium vacancy changed more significantly under homogeneous strain than that of a di-vacancy cluster. Further, based on our simulations of both single and di-vacancies, we observe that the individual paths interact differently to the applied strain, i.e. the changes in their barrier height are different, depending on the magnitude and direction of applied strain. We also find that the effect of external strain on diffusivity depend on the charge state of the defect,as neutral defects tend to have larger components in their relative dipole tensor ($\Delta G_{ij}^{\text{mig}}$) than charge defects and thus interact with strain field more strongly. This work provides the foundation to analyze other defects (such as interstitials, fission gases, fission products etc.) and their interaction with much more complex strain fields, due to dislocations, dislocation loops, grain boundaries and other microstructural features individually or in combination, as function of temperature and relatively longer times via KMC simulations. The stoichiometry of UO_2 can affect the concentration of various defect types in the fuel and therefore, studying different vacancy types, both in charged and neutral configurations, can provide insight into the diffusion behavior of defects in different chemical environments. All of this information is important for building physical models of the evolution of the fuel in service.

Finally, these results have important implications for mass transport in fluorite structured oxides[29–31], beyond the specific material studied here, in which mechanical strains have been proposed as a new means of enhancing ionic conductivity. For example, an experimental study[31] on YSZ has shown about 18% improvement in oxygen ion mobility under tensile stresses, with improvement more prominent at relatively lower temperatures. Many applications of oxides involve complex strain states, including thin film geometries and nanocomposites[25–28]. Our results show that the coupling between strain and diffusion can be rather complex, with significant changes in mobility in directions perpendicular to the applied strains. For example, vertical strains are shown to dominate the overall strain state in epitaxial thin film composites[27] with thickness over 20 nm, promising greater control of functional properties beyond those typical of the lateral strains in such films. In applications involving zirconia and hafnia-based advanced thermal barrier coatings[32,33], it is reported that thermal gradients result in strains and strain gradients, which ultimately affect metal cation diffusivities. Therefore knowledge of ionic diffusivity as a function of strain aids in understanding both creep as well as sintering rates and, hence, in predicting the durability these coatings.

To conclude, this work provides a link between atomistic simulations and mesoscale representations of the material. Diffusion is an average property, accounting for the effect of strain on all possible paths and their transition states. Dipole tensors for all defects and their transition states have been calculated from DFT calculations, which formed the basis of KMC simulations that can account for changes in behavior with strain and average these changes over all pathways in the system. That said, there are still several outstanding and important questions, such as what is the effect of the magnetic state and intermediate charge states of defects in UO_2 on the nature of the dipole tensor. Questions, pertaining to the nature dipole tensor, such as how sensitive each element of the dipole tensor is to the underlying symmetry of the distorted fluorite structure also warrant further investigation. In summary, the coupling of DFT calculations and KMC simulation via the dipole tensor approach used in this study provides an extensive and systematic assessment of the effect of homogeneous strains (within linear elasticity) on the diffusivity of uranium single and divacancies in UO_2. Our results can also provide physical parameter for higher length scale model to predict and understand fuel mechanical behavior.

Appendix A

A single uranium vacancy can migrate to it twelve nearest neighbors along ⟨110⟩. As discussed in Sec. II, the uranium vacancy migration path is complicated, involving two saddles (S1 and S2 in Figure 16) along a curved path (Figure 4), rather than a simple transition between nearest uranium sites along ⟨110⟩ directions. Given a two-fold symmetry along ⟨110⟩ direction and the curved migration path, each migration direction actually consists of four paths, making a total of forty-eight possible paths for uranium vacancy to migrate to it nearest neighbor position along ⟨110⟩ direction. To obtain a full KMC catalog of dipole tensors for single uranium vacancies (involving forty-eight paths and ninety-six saddles, as each path has two saddles), we performed symmetry operations on the dipole tensor of the saddle from the DFT calculations, to obtain dipole tensors for all other

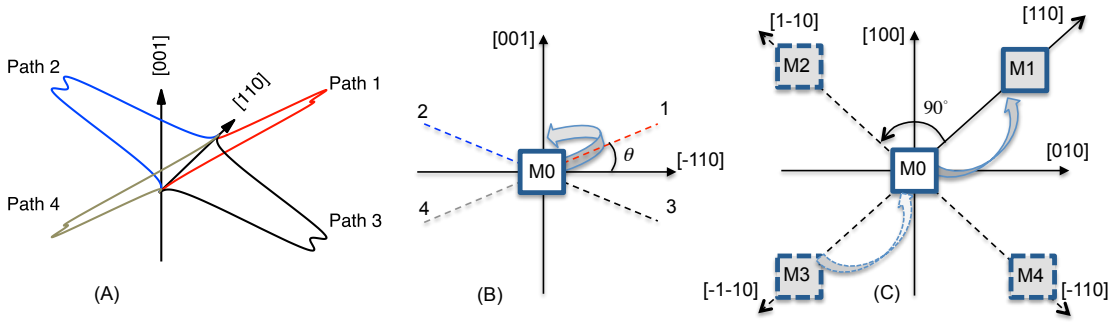

FIG. 16. (A) schematic of four equivalent paths along one particular [110] direction. (B) Schematic diagram of how to obtain the dipole tensors for four paths along a specific [110] direction, which is a two-fold symmetry direction in UO_2. Path 2 is obtained by reflection in the $(\bar{1}10)$ plane of path 1, and path 3 and 4 are obtained by reflection of path 1 and 2 though the (001) plane, respectively. (C) Schematic for obtaining all in-plane dipole tensors corresponding to other $\langle 110 \rangle$ directions in the (001) plane, namely $[1\bar{1}0]$, $[\bar{1}\bar{1}0]$ and $[\bar{1}10]$ by in-plane rotation of 90 ° about the four-fold [001] axis. Vacancy sites (or minima) are shown as M0, M1, M2 and M3.

symmetrically equivalent paths. These symmetry operations can be characterized by performing simple tensor operations, defined as

$$\bar{\boldsymbol{A}} = \boldsymbol{RAR^T} \tag{A1}$$

where $\mathbf{A}$ is any second-rank tensor and $\bar{\boldsymbol{A}}$ is the final resultant tensor after applying the symmetry operation. $\mathbf{R}$ is the reflection or rotation matrix depending on the specific symmetry operation and $\boldsymbol{R^T}$ is its corresponding transpose. In our calculations, the general form of matrix $\mathbf{R}$, involving rotation about an axis oriented along a arbitrary unit vector $\langle u, v, w \rangle$ by angle θ is given by transformation matrix $\mathbf{R}$.[89] First, we apply symmetry operations to obtain dipole tensors for both saddles for the four-degenerate path along a single [110] direction, followed by symmetry operations to obtain the dipole tensor of the saddles for all the remaining in-plane and out-of-plane directions. As shown in Figure 16, paths 1, 2, 3 and 4 corresponds to transition from the initial state M0 to final state M1 along [110]. Dipole tensors for path 1 when reflected through the $(\bar{1}10)$ and (001) planes give dipole tensors for path 2 and 3, respectively, and the dipole tensors for path 4 can be obtained by reflection of path 2 across the (001) plane. In-plane dipole tensors along $[1\bar{1}0]$ (M0 → M2), $[\bar{1}\bar{1}0]$ (M0 → M3) and $[\bar{1}10]$ (M0 → M4) are obtained by rotating path 1 (M0 → M1) by 90°, 180° and 270°, respectively around the [001] axis, followed by the same set of reflections as for [110] (M0 → M1), to obtain dipole tensors for all equivalent paths along those directions. Out-of-plane dipole tensors, i.e. for planes (100) and (010), are obtained by 90° clockwise rotation of [110] (M0 → M1) around [010] and 90° anti clockwise rotation of [110] (M0 → M1) around [100], respectively.

$$\mathbf{R} = \begin{bmatrix} u^2 + (1-u^2)cos\theta & uv(1-cos\theta) - wsin\theta & uw(1-cos\theta) + vsin\theta & 0 \\ uv(1-cos\theta) + wsin\theta & v^2 + (1-v^2)cos\theta & vw(1-cos\theta) - usin\theta & 0 \\ uw(1-cos\theta) - vsin\theta & vw(1-cos\theta) + usin\theta & w^2 + (1-w^2)cos\theta & 0 \\ 0 & 0 & 0 & 1 \end{bmatrix} \tag{A2}$$

ACKNOWLEDGMENTS

AG is happy to acknowledge the Materials Science and Technology Division at Los Alamos National Laboratory for hospitality during this project. The work of AG and SRP was supported by the DOE-NE Nuclear Energy University Program 10-2258. This work is also funded by the Department of Energy Nuclear Energy Advanced Modeling and Simulation (NEAMS) program.

* anuj.goyal@ufl.edu
† blas@lanl.gov

[1] D. Olander, *Fundamental aspects of nuclear reactor fuel elements* (Technical Information Center, Energy Research

and Development Administration, 1976).
[2] D. Olander, Journal of Nuclear Materials **389**, 1 (2009).
[3] R. Devanathan, L. Van Brutzel, A. Chartier, C. Guéneau, A. E. Mattsson, V. Tikare, T. Bartel, T. Besmann, M. Stan, and P. Van Uffelen, Energy & Environmental Science **3**, 1406 (2010).
[4] H. Stehle, H. Assmann, and F. Wunderlich, Nuclear Engineering and Design **33**, 230 (1975).
[5] W. R. Cannon and T. G. Langdon, Journal of Materials Science **18**, 1 (1983).
[6] R. W. Davidge and A. G. Evans, Journal of nuclear materials **33**, 249 (1969).
[7] J. Weertman, ASM TRANS QUART **61**, 681 (1968).
[8] A. Solomon, Journal of the American Ceramic Society **56**, 164 (1973).
[9] W. Dienst, Journal of Nuclear Materials **65**, 1 (1977).
[10] J. H. Gittus, Philosophical Magazine **25**, 345 (1972).
[11] M. Seltzer, A. Clauer, and B. Wilcox, Journal of Nuclear Materials **44**, 43 (1972).
[12] F. A. Mohamed and M. S. Soliman, Materials Science and Engineering **53**, 185 (1982).
[13] O. Ruano, J. Wolfenstine, J. Wadsworth, and O. Sherby, Acta Metallurgica et Materialia **39**, 661 (1991).
[14] J. Gao, L. Wang, Y. Wang, and S. Wu, Transactions of Nonferrous Metals Society of China **20**, 238 (2010).
[15] J. Wang and T. Nieh, Journal of Nuclear Materials **228**, 141 (1996).
[16] F. A. Mohamed and T. J. Ginter, Acta Metallurgica **30**, 1869 (1982).
[17] A. Solomon, C. Yust, and N. Packan, Journal of Nuclear Materials **110**, 333 (1982).
[18] H. Frost and M. Ashby, *Deformation mechanism maps: the plasticity and creep of metals and ceramics* (Pergamon Press, 1982).
[19] D. Knorr, R. Cannon, and R. Coble, Acta Metallurgica **37**, 2103 (1989).
[20] D. A. Andersson, B. P. Uberuaga, P. V. Nerikar, C. Unal, and C. R. Stanek, Physical Review B **84**, 1 (2011).
[21] D. A. Andersson, P. Garcia, X. Liu, G. Pastore, M. Tonks, P. Millett, B. Dorado, D. R. Gaston, D. Andrs, R. L. Williamson, R. C. Martineau, B. P. Uberuaga, and C. R. Stanek, Journal of Nuclear Materials **451**, 225 (2014).
[22] B. Dorado, D. Andersson, C. Stanek, M. Bertolus, B. Uberuaga, G. Martin, M. Freyss, and P. Garcia, Physical Review B **86**, 035110 (2012).
[23] G. Subramanian, D. Perez, B. P. Uberuaga, C. N. Tomé, and A. F. Voter, Physical Review B **87**, 144107 (2013).
[24] K. E. Sickafus, E. Kotomin, and B. P. Uberuaga, *Radiation Effects in Solids*, edited by K. E. Sickafus, E. A. Kotomin, and B. P. Uberuaga, NATO Science Series, Vol. 235 (Springer Netherlands, Dordrecht, 2007).
[25] J. Garcia-Barriocanal, A. Rivera-Calzada, M. Varela, Z. Sefrioui, E. Iborra, C. Leon, S. J. Pennycook, and J. Santamaria, Science **321**, 676 (2008).
[26] T. J. Pennycook, M. J. Beck, K. Varga, M. Varela, S. J. Pennycook, and S. T. Pantelides, Physical Review Letters **104**, 115901 (2010).
[27] J. L. MacManus-Driscoll, J. L. MacManus-Driscoll, P. Zerrer, P. Zerrer, H. Wang, H. Wang, H. Yang, H. Yang, J. Yoon, J. Yoon, A. Fouchet, A. Fouchet, R. Yu, R. Yu, M. G. Blamire, M. G. Blamire, Q. Jia, and Q. Jia, Nature materials **7**, 314 (2008).
[28] N. Schichtel, C. Korte, D. Hesse, and J. Janek, Physical chemistry chemical physics : PCCP **11**, 3043 (2009).
[29] X.-M. Bai, Y. Zhang, and M. R. Tonks, Physical chemistry chemical physics : PCCP **15**, 19438 (2013).
[30] M. J. D. Rushton and a. Chroneos, Scientific Reports **4**, 2 (2014).
[31] W. Araki, Y. Imai, and T. Adachi, Journal of the European Ceramic Society **29**, 2275 (2009).
[32] D. Zhu and R. a. Miller, Surface and Coatings Technology **108-109**, 114 (1998).
[33] K. Knipe, A. Manero, S. F. Siddiqui, C. Meid, J. Wischek, J. Okasinski, J. Almer, A. M. Karlsson, M. Bartsch, and S. Raghavan, Nature communications **5**, 4559 (2014).
[34] G. Kresse and J. Hafner, Physical Review B **48**, 13115 (1993).
[35] G. Kresse and J. Furthmüller, Computational Materials Science **6**, 15 (1996).
[36] G. Kresse and J. Furthmüller, Physical Review B **54**, 11169 (1996).
[37] G. Kresse and D. Joubert, Physical Review B **59**, 1758 (1999).
[38] P. E. Blöchl, Physical Review B **50**, 17953 (1994).
[39] A. I. Liechtenstein, V. I. Anisimov, and J. Zaanen, Physical Review B **52**, R5467 (1995).
[40] G. Henkelman, B. P. Uberuaga, and H. Jonsson, The Journal of Chemical Physics **113**, 9901 (2000).
[41] M. Allen and D. Tildesley, *Physics Today* (Oxford University Press, USA (June 29, 1989), 1989).
[42] T. Arima, K. Yoshida, K. Idemitsu, Y. Inagaki, and I. Sato, IOP Conference Series: Materials Science and Engineering **9**, 012003 (2010).
[43] A. S. Boyarchenkov, S. I. Potashnikov, K. A. Nekrasov, and A. Y. Kupryazhkin, Journal of Nuclear Materials **442**, 148 (2013).
[44] R. Veiga, M. Perez, C. Becquart, E. Clouet, and C. Domain, Acta Materialia **59**, 6963 (2011).
[45] A. Nowick and B. Berry, *Journal of Polymer Science: Polymer Letters Edition*, Vol. 11 (Academic Press, New York, 1972).
[46] M. J. Gillan, Philosophical Magazine A **48**, 903 (1983).
[47] M. J. Gillan, Journal of Physics C: Solid State Physics **17** (1984).
[48] E. Clouet, S. Garruchet, H. Nguyen, M. Perez, and C. S. Becquart, Acta Materialia **56**, 3450 (2008).
[49] M. R. Sorensen and A. F. Voter, The Journal of Chemical Physics **112**, 9599 (2000).
[50] D. Matsunaka and Y. Shibutani, Journal of physics. Condensed matter : an Institute of Physics journal **23**, 265008 (2011).
[51] G. Vineyard, Journal of Physics and Chemistry of Solids **3**, 121 (1957).
[52] M. Leslie and M. J. Gillan, Journal of Physics C: Solid State Physics **18**, 973 (1985).
[53] A. S. Nowick and W. Heller, Advances in Physics **12**, 251 (1963).
[54] J. R. Hardy and A. B. Lidiard, Philosophical Magazine **15**, 825 (1967).
[55] H. Kanzaki, Journal of Physics and Chemistry of Solids **2**, 24 (1957).
[56] D. A. Freedman, D. Roundy, and T. Arias, Physical Review B **80**, 064108 (2009).
[57] M. Sanati, R. C. Albers, T. Lookman, and A. Saxena, Physical Review B **84**, 014116 (2011).
[58] P. H. Dederichs, C. Lehmann, and a. Scholz, Zeitschrift fr Physik B: Condensed Matter and Quanta **20**, 155 (1975).
[59] M. P. Puls, Philosophical Magazine A **51**, 893 (1985).

[60] G. Ackland, Journal of Nuclear Materials **152**, 53 (1988).
[61] J. Hinterberg, T. Zacherle, and R. A. De Souza, Physical Review Letters **110**, 205901 (2013).
[62] A. Lidiard, Journal of Nuclear Materials **19**, 106 (1966).
[63] J. Belle, Journal of Nuclear Materials **30**, 3 (1969).
[64] H. Matzke, Journal of the Chemical Society, Faraday Transactions 2 **83**, 1121 (1987).
[65] A. Sabioni, W. Ferraz, and F. Millot, Journal of Nuclear Materials **257**, 180 (1998).
[66] P. Nerikar, T. Watanabe, J. S. Tulenko, S. R. Phillpot, and S. B. Sinnott, Journal of Nuclear Materials **384**, 61 (2009).
[67] M. Freyss, T. Petit, and J.-P. Crocombette, Journal of Nuclear Materials **347**, 44 (2005).
[68] J. P. Crocombette, F. Jollet, L. Nga, and T. Petit, Physical Review B **64**, 104107 (2001).
[69] J.-P. Crocombette, D. Torumba, and A. Chartier, Physical Review B **83**, 184107 (2011).
[70] M. Cherry, M. Islam, and C. Catlow, Journal of Solid State Chemistry **118**, 125 (1995).
[71] S. Boyapati, E. D. Wachsman, and N. Jiang, Solid State Ionics **140**, 149 (2001).
[72] D. S. Aidhy, S. B. Sinnott, E. D. Wachsman, and S. R. Phillpot, Ionics **16**, 297 (2010).
[73] B. Dorado, G. Jomard, M. Freyss, and M. Bertolus, Physical Review B **82**, 035114 (2010).
[74] A. M. Stoneham, Contemporary Physics **20**, 535 (1979).
[75] R. Laskowski, G. K. H. Madsen, P. Blaha, and K. Schwarz, Physical Review B **69**, 140408 (2004).
[76] P. Santini, S. Carretta, G. Amoretti, R. Caciuffo, N. Magnani, and G. Lander, Reviews of Modern Physics **81**, 807 (2009).
[77] B. Dorado and P. Garcia, Physical Review B **87**, 195139 (2013).
[78] M. Rushton, A. Chroneos, S. Skinner, J. Kilner, and R. Grimes, Solid State Ionics **230**, 37 (2013).
[79] K. Ramakrishnan, Journal of materials science letters **8**, 269 (1999).
[80] V. Borodin and a.I. Ryazanov, Journal of Nuclear Materials **210**, 258 (1994).
[81] R. Bullough and R. C. Newman, Reports on Progress in Physics **33**, 101 (1970).
[82] C. Woo and U. Gösele, Journal of Nuclear Materials **119**, 219 (1983).
[83] A. Brailsford, Philosophical Transactions of the Royal Society of London. Series A, Mathematical and Physical Sciences **302**, 87 (1981).
[84] P. Nerikar, D. Parfitt, L. Casillas Trujillo, C. Andersson, D. A.and Unal, S. Sinnott, R. Grimes, B. P. Uberuaga, and C. R. Stanek, Physical Review B **84**, 174105 (2011).
[85] A. Goyal, T. Rudzik, B. Deng, M. Hong, A. Chernatynskiy, S. B. Sinnott, and S. R. Phillpot, Journal of Nuclear Materials **441**, 96 (2013).
[86] J. Gittus, D. Howl, and H. Hughes, Nuclear applications and technology **9**, 40 (1970).
[87] R. F. Canon, J. T. A. Roberts, and R. J. Beals, Journal of the American Ceramic Society **54**, 105 (1971).
[88] A. Debelle, A. Boulle, F. Garrido, and L. Thomé, Journal of Materials Science **46**, 4683 (2011).
[89] G. B. Arfken and H. J. Weber, *Mathematical Methods for Physicists*, Mathematical Methods for Physicists (Elsevier, 2005).